Available online at www.sciencedirect.com

ScienceDirect

Materials Today: Proceedings 6 (2019) 270–278

materialstoday: PROCEEDINGS

www.materialstoday.com/proceedings

3rd ISE SSRSEU 2018

Pure ultrafine magnetite from carbon steel wastes

O. Butenko[a], V. Boychuk[b], B. Savchenko[a], V. Kotsyubynsky[b], V. Khomenko[a] and V. Barsukov[a*]

[a]*Kyiv National University of Technologies and Design, 2 Nemyrovych-Danchenka str., Kyiv 01011, Ukraine*
[b]*Vasyl Stefanyk Precarpathian National University, 57 Shevchenko Str., Ivano-Frankivsk 76025, Ukraine*

Abstract

This paper proposes a straightforward air-aqueous oxidation of St3 steel wastes for mass production of pure ultrafine magnetite. The characterization of the obtained product has been made by X-ray fluorescence analysis, X-ray diffraction, impedance spectroscopy, low-temperature nitrogen absorption method, Mössbauer spectroscopy and optical microscopy. The investigation results have shown high purity of the obtained product, wide range of particle sizes and strongly pronounced magnetic properties.

Selection and peer-review under responsibility of the scientific committee of 3rd ISE Satellite Student Regional Symposium on Electrochemistry in Ukraine.

Keywords: ultrafine magnetite, X-ray diffraction, Mössbauer spectroscopy, EDXRF, electrical conductivity

1. Introduction

Magnetite powders with different degrees of dispersion are used in production of active materials for alkaline batteries, magnetic fluids, ferrites, catalysts, as well as for defectoscopy, multifunctional diagnostics in biology and medicine, in particular for the targeted delivery of medicinal products and the hyperthermia approach to treating cancer (e. g. [1]). In chemical methods of magnetite synthesis the following approaches (in various modifications) are commonly used.

1) Fe^{2+}, Fe^{3+} ions co-precipitation in alkaline medium by mixing salt solutions;
2) Heating the fine powder of Fe_2O_3 in a stream of nitrogen (at 400 ℃) with further replacement of the nitrogen with hydrogen saturated with water vapor (about 5 hours) until the final reduction of the powder [2].

* Corresponding author. Tel.: +38-067-504-4565 fax: +38-044-284-8266
E-mail address: v-barsukov@i.ua

Selection and peer-review under responsibility of the scientific committee of 3rd ISE Satellite Student Regional Symposium on Electrochemistry in Ukraine.

The complexity and high cost of the technology, lack of the final product purity (especially in (1) due to the duration and complexity of the product washing) are disadvantages of such approaches. At the same time, under the conditions of natural corrosion of carbon steel, rust is formed on the surface, which can contain a rather large part of magnetite. The aim of this work is to develop a method for preparation of ultrafine magnetite on the basis of natural "rust", determination of purity, structure, magnetic and electrical conductive properties, particle size distribution and other characteristics of such a product.

2. Experimental details

2.1. *Preparation of ultrafine magnetite*

Samples of St3 steel (such as E 235-A, Fe 360-A, etc.) produced by the PJSC "Arcelor Mittal Kryvyi Rih" (Ukraine) were studied. Numerous foreign analogues of this commonly used steel brand are listed below [3]. The tentative chemical composition of the St3 steel was the following (Table 1 [3]):

Table 1. The tentative chemical composition of the initial St3 steel from the "Arcelor Mittal Kryvyi Rih" (Ukraine) and its foreign analogues

Element	Fe	C	Si	Mn	Ni	S	P	Cr	Cu	As	N
%	~97.0	0.14…0.22	0.15…0.30	0.40…0.65	<0.30	<0.05	<0.04	<0.30	<0.30	<0.08	<0.008

Iron oxide was formed on the surface of St3 steel wastes by the cyclic action of moisture and air. The depth of oxidation (corrosion) of samples ranged from 0.5 to 2.0 mm. The iron oxide particles were separated from the surface by mechanical treatment (stapling), washed with water and dried in a drying oven at 120°C for 6 hours. After that, preliminary grinding was performed in a porcelain mortar to a particle size of 1 - 2 mm. Further, the oxide particles were ground with a Fritsch Pulverisette 2mortar mill. The grinding time was 30 minutes. The load weight was 80 g.

2.2. Materials characterization

Structure characterization was carried out by powder X-ray diffraction (XRD) with a DRON-4-07 diffractometer (Cu K_α radiation, 40 kV, 30 mA) Bragg-Brentano geometry at room temperature. A qualitative analysis was carried out using ICSD structural models. Copper powder, vacuum annealed at 850 - 900°C for 4 h, with an average grain size of about 50 μm was used as a reference sample to determine the instrumental peak broadening. The Scherrer equation was used for obtaining information about the average size of the coherently scattering domains:

$$D = \frac{K\lambda}{\beta \cos\theta},$$

where K is the shape factor (K = 0.89), λ is the wavelength (0.15405 nm), β is the full width at half maximum of peaks in radian and 2θ is the peak position on the diffraction pattern.

Frequency dependencies of electrical conductivity, σ, were measured by the impedance spectroscopy method (Autolab PG-STAT 12/FRA-2 device) in a temperature range of 20-150°C. Samples for electrical conductivity tests had a form of cylindrical pellet with a diameter of $17 \cdot 10^{-3}$ m and thickness of $(0.10\text{-}0.15) \cdot 10^{-3}$ m under pressure of about 30-35 MPa at room temperature. Specific surface area was measured by the low-temperature nitrogen absorption method (Quantachrome Autosorb Nova 2200e device). Mössbauer investigation in transmission geometry was carried out at room temperature using an MS1104Em spectrometer (isomeric shift calibration relative to α-Fe, the velocity resolution 0.006 mm/s per channel). To determine the particle size distribution, an optical microscopic analysis was performed using an IMM 901 inverted metallurgical microscope with a digital camera. The ImageJ program package was used for image processing and automatic determination of particle size distributions. The chemical composition of magnetite powders was analyzed with an Energy Dispersive X-ray

fluorescence (EDXRF) spectrometer (X-Supreme8000, Oxford Instruments) consisting of a Si detector and X-ray tubes with Pd target.

3. 3. **Results and discussions**

The XRD pattern (Fig. 1, a) of the prepared iron oxide sample shows the presence of magnetite (PDF, No 01-075-0449) and goethite (PDF, No 00-003-0249) phases in a ratio of about 45:55 mass. %. The average crystallite size of magnetite is about 21nm. The broadening of reflexes on the XRD pattern of goethite occurs due to relatively smaller particle sizes. According to theoretical random particle distribution, the ratio of integrated intensities (pseudo-Voight approach) for the (110) and (111) peaks is about 1.25 [4], whereas our calculated value is 0.85-0.90, which predicts goethite crystals preferable growth along the (111) direction. Typically, goethite microcrystals are characterized by the (110) form but hydrothermal synthesis conditions lead to formation of more complex morphology, which affects the material properties [5]. The presence of the (111) facets may suggest asymmetric and rounded growth way and formation of spiral twisted particles (fig.1, b) [6]. The observed increase in the (120) peak intensity agrees with the proposed model of particle spiral growth. The average crystallite size of goethite is about 10-12 nm (calculation using FWHM of (110) and (111) reflexes). In the case of complex particle morphology this value has only evaluative character. The XRD pattern contains additional peaks in an angular range of 2θ=48-52°, which does not correspond to magnetite and goethite structures. This may be due to goethite first stage transformation into a hematite-like non-stoichiometric phase like α-$Fe_{2-x/3}$-$(OH)_xO_{3-x}$. [7]. At the same time, the appearance of these peaks can be explained by the complex morphology of goethyte particles.

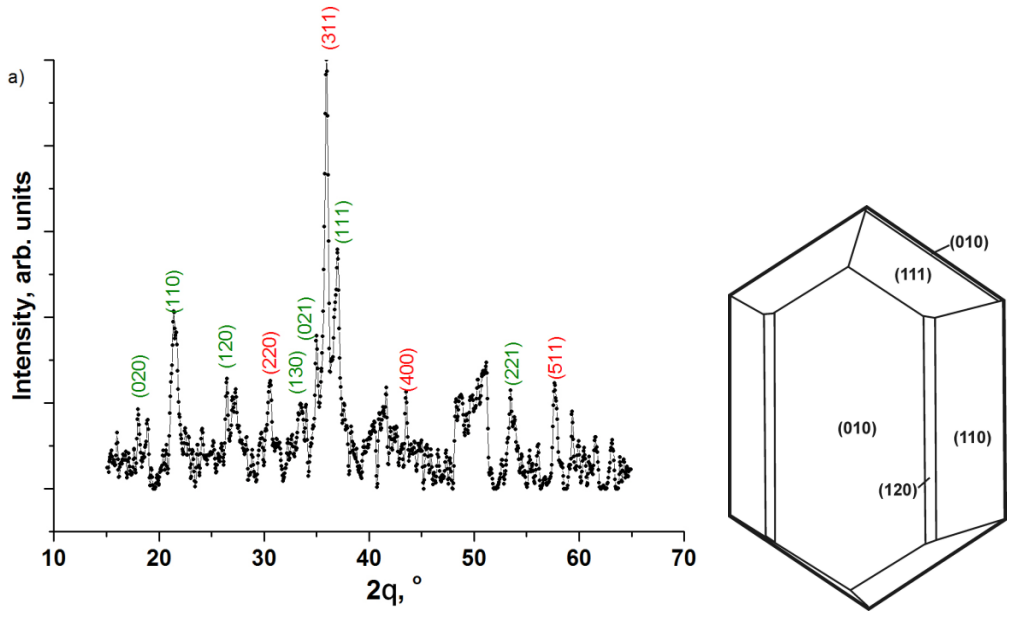

Fig.1. XRD pattern of iron oxide sample (a) and schematic representation of the morphology of a goethite monocrystal (b).

Independent information about phase contents, magnetic microstructure and the valence states of iron ions was obtained by Mössbauer spectroscopy (fig.2). The magnetic properties of ultrafine iron oxide are known to be strongly dependent on the crystallite sizes and inter-particle interaction [8]. The complex Mössbauer spectra were optimally approximated by superposition of 10 sextets – 2 sextets correspond to different sublattices of Fe_3O_4 and the other 8 sextet components correspond to the ^{57}Fe nuclei with different crystallographic surroundings located in goethite nanoparticles (Table 2).

The component of magnetite spectra with values of hyperfine magnetic fields on the ^{57}Fe corresponds to the Fe^{3+} located in the tetrahedral sublattice and both Fe^{3+} and Fe^{2+} located in the octahedral sublattice. Magnetite exhibits

percolation electron conductivity via fast electron hopping between octahedral coordinated iron ions at room temperature. The characteristic time of hopping is short compared to the characteristic lifetime of the excited state of the ^{57}Fe nucleus, so iron ions with an average valence state of 2.5+ are observed in the octa-sublattice [9].

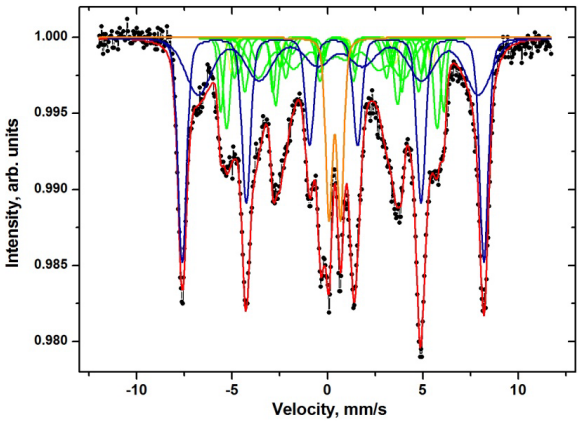

Fig. 2. Mössbauer spectra of synthesized material

Table 2. Parameters of Hyperfine Interactions for Synthesized Iron Oxide (hyperfine magnetic field H_{hf} , isomer shift I_s, quadrupole splitting Q_s, line width G, integral intensity S)

		I_s, mm/s	Q_s, mm/s	H, kOe	S, %	G, mm/s
1	α-FeOOH-8,360	0.381	-0.274	363.0	5.6	0.326
2	α-FeOOH-7,345	0.354	-0.246	342.7	8.9	0.437
3	α-FeOOH-6,330	0.365	-0.320	327.5	2.3	0.319
4	3.1.1. α-FeOOH-5,315	0.322	-0.280	314.2	3.3	0.326
5	α-FeOOH-4,300	0.313	-0.375	298.0	3.5	0.436
6	α-FeOOH-3,285	0.338	-0.227	282.9	4.9	0.430
7	α-FeOOH-2, 255	0.408	-0.175	252.0	2.7	0.460
8	α-FeOOH-1, 240	0.313	-0.266	237.0	10.8	1.169
9	Fe_3O_4,(Fe^{3+})	0.307	-0.031	491.2	29.4	0.539
10	Fe_3O_4,[Fe^{2+}, Fe^{3+}]	0.620	-0.102	456.1	22.1	1.628
11	α-FeOOH-0	0.381	0.603	–	6.5	0.422

The comparison of relative integral intensity of these two components of magnetite spectra allows one to calculate its stoichiometry as [10]:

$$x_{ms} = \frac{Fe^{2+}}{Fe^{3+}} = \frac{\frac{1}{2} Fe^{2.5+}_{oct}}{\frac{1}{2} Fe^{2.5+}_{oct} + Fe^{3+}_{oct,tet}}.$$

The reduction of the average particle size leads to an increase in the oxidation degree and a decrease in x_{ms} due to the $Fe^{2.5+}$ sextet integral intensity decreasing simultaneously with the $Fe^{3+}{}_{Oct,Tet}$ sextet enlarging. In our case, $x_{ms} = 0.273$ when $x_{ms} = 0.50$ for stoichiometric magnetite. The decrease in x_{ms} leads to formation of cationic vacancies and a decrease in the unit cell due to a smaller ionic radius for Fe^{3+} ions compared to Fe^{2+} and transformation of magnetite to maghemite $Fe_{3-\delta}O_4$ or ${}^{tet}Fe^{3+}\left[{}^{oct}Fe^{2+}_{1-3\delta}\,{}^{oct}Fe^{3+}_{1+2\delta}\square_{\delta}\right]O_4$, where □ are the vacancies formed for charge balance and δ is in the range from 0 (stoichiometric magnetite) to 0.333 (completely oxidized magnetite).

The stoichiometry, δ, calculated as $\delta = \frac{1-2x_{ms}}{2x_{ms}+3}$, for the synthesized material is 0.128. The stoichiometry of magnetite determines its conductivity, crystalline structure and electrochemical properties.

Our using eight different sub-spectra for describing the goethite component of the material is explained by its nonstoichiometry, which causes broadening resonant lines. There is a continuous distribution of hyperfine magnetic field on the ^{57}Fe nuclei from maximal value and up to the superparamagnetic state [11]. In our investigations the relative content of ^{57}Fe in the superparamagnetic state located in the goethite particles is about 6.2 %.

The hyperfine field distribution *vs* relative integral intensity of the sextet component with this value of H_{hf} for goethite nanoparticles was plotted as histograms (fig.3).

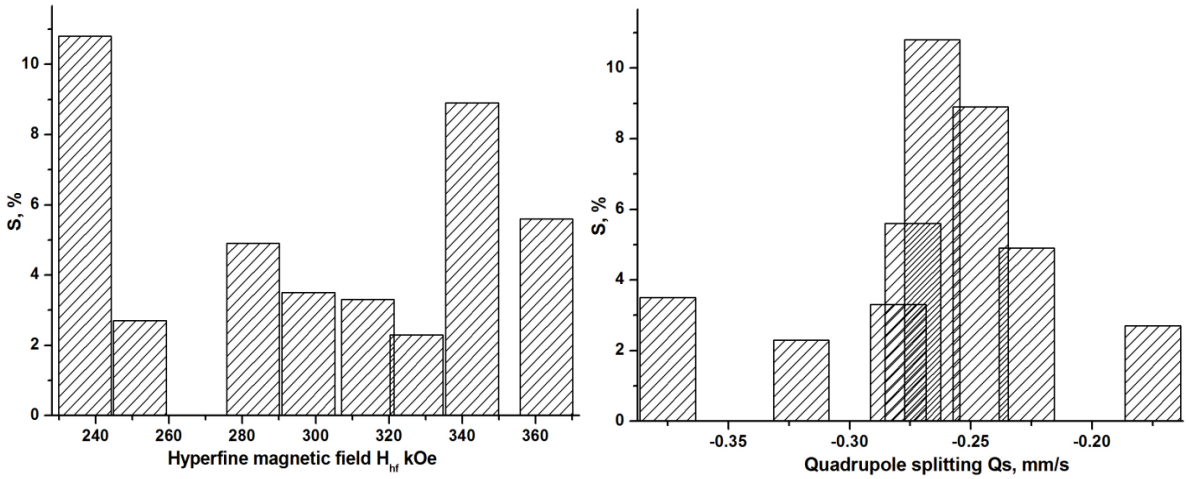

Fig.3. Hyperfine field distributions for goethite component of syntesized material

It was determined that the formation of defect states with the largest hyperfine fields (about 340-360 kOe) is most probable. The presence of the ^{57}Fe nuclei with hyperfine fields of about 230-240 kOe for defect goethite corresponds to conclusions in [12]. It is clear that quadrupole splitting determined by the symmetry of the ^{57}Fe near surroundings is also a function of crystalline imperfections, so the dependencies of sextet component integral intensity vs these parameters were analyzed (Fig 3,b). The most probable value of quadruple splitting is about -0.25 mm/s. Both magnetite and goethite have semiconductor properties but conductivity of Fe_3O_4 at room temperature is 10^6-10^7 times higher than that of the α-FeOOH. The electrical conductivity of magnetite is determined by fast electron hopping between octahedrally coordinated Fe^{2+} and Fe^{3+} ions with an activation energy of about 0.05 eV [13], whereas the activation energy of conductivity for goethite is about 2.6 eV [14]. Fig. 4 shows frequency dependencies of σ_{ac} for a magnetite sample at different temperatures. An increase in DC conductivity of pure magnetite with temperature is expected but, experimentally, a systematic decrease in this parameter was observed. The decrease in DC conductivity in the investigated temperature range can be explained by thermally induced velocities of charge carriers prevailing over their drift velocity induced by the electric field [13]. The electrical conductivity of magnetite, according to Koop's theory [15], exhibits dispersion at frequencies higher than 10^4 Hz, which corresponds to the presence of grains with high inner conductivity and high resistance boundaries. The increasing conductivity at high frequencies is due to the enlarged hopping probability of charge carriers. The frequency dependencies of σ at different temperatures were fitted using the Jonscher's power law: $\sigma(\omega) = \sigma_{dc}\left[1+\left(\frac{\omega}{\omega_h}\right)^s\right]$, where σ_{dc} is the dc conductivity, ω_h is the hopping frequency of the charge carriers, s is the frequency exponent parameter ($0 < s < 1$), which is a measurement of the inter-ionic coupling strength [16].

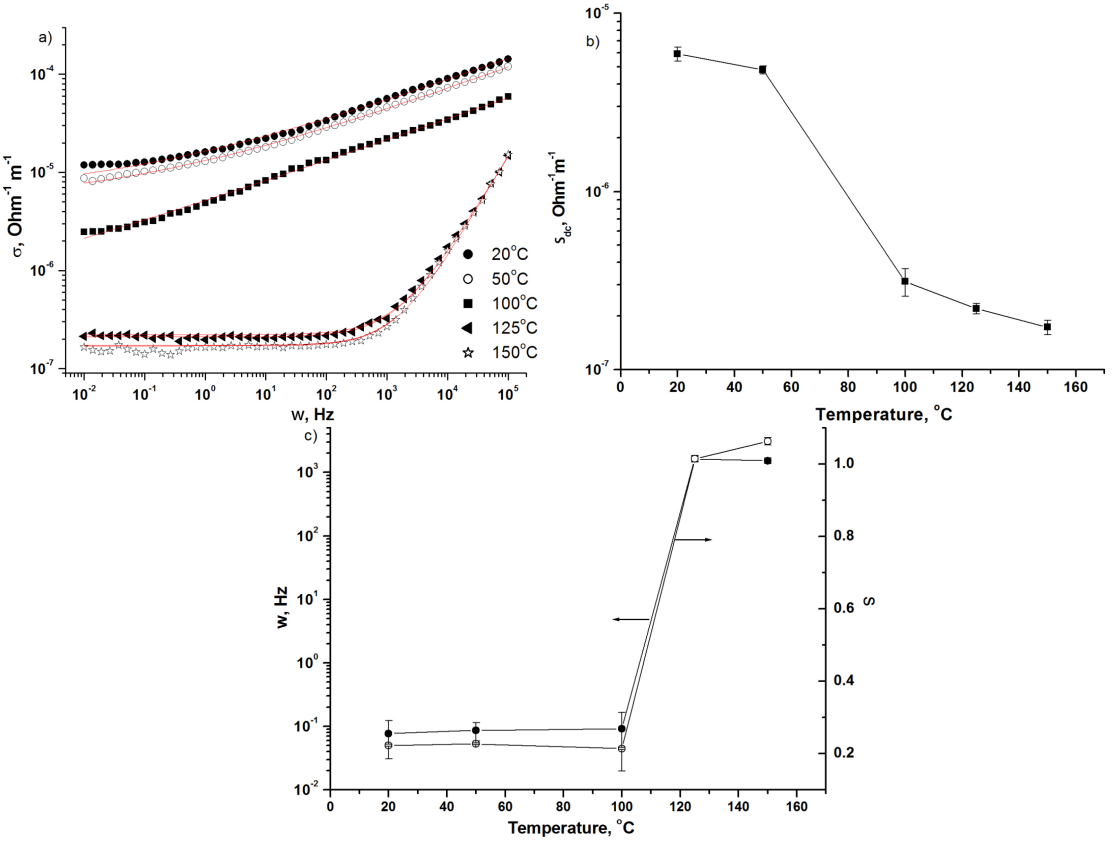

Fig.4. Frequency dependencies of electrical conductivity measured for the obtained iron oxide material with solid lines corresponding to the fitting power law by Jonscher's (a); DC conductivity vs temperature, calculated based on Jonscher's power law (b) and temperature dependencies of hopping frequencies and value of the exponent s (c)

The analysis of the *s*(T) dependency (fig. 4, c) allows investigation of conduction mechanism under the applied AC field. There is no change in the exponent *s* value up to 100°C, which corresponds to a very slow frequency dependency of conductivity. A sharp jump of the s parameter in the 100-125°C temperature range was observed with the next stabilization of this value close to 1. There are some theoretical models that explain frequency and temperature dependencies of electrical conductivity for this case. One of them is the correlated barrier hopping (CBH) model, which can be associated with charge carriers exchange process between the Fe^{3+} and Fe^{2+} ions in magnetite structure. The increasing AC frequency caused the enlarging probability of electronic hops between localized states. The CBH theory predicts the declining character of s (T) but, according to the Koop's theory, resistance of the grain boundaries can cause the plateau region formation [16]. The increase in s with temperature can be explained by non-overlapping small polaron tunneling (NSPT) mechanisms of conductivity [17], which is associated with small polaron formation during electrostatic lattice deformation at charge carrier transfer. The values of s exponent close to 1 at temperatures ≥125°C correspond closely to the ideal Debye dielectric dipolar crystals [18].

The hopping energy W_h was calculated using the values of s exponent at different temperatures according to the CBH and NSPT models (Fig. 5) as: $W_h = kT\left[\ln\left(\frac{1}{\omega\tau_0}\right) - \frac{4}{1-n}\right]$, where *k* is the Boltzmann constant, T is the temperature, ω is the circular frequency ($\omega = 2\pi f$), τ_0 is the characteristic relaxation time equal to $\tau_0 = 10^{-13}$ s [19].

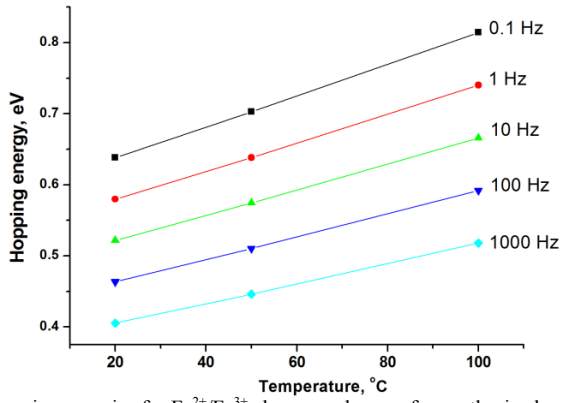

Fig.5. Temperature dependencies of hopping energies for Fe^{2+}/Fe^{3+} charge exchanges for synthesized material at different frequencies

The chemical composition of the synthesized material has been investigated by EDXRF. Figure 6 shows a typical fluorescence spectrum of this material obtained with a EDXRF spectrometer. It is evident from the spectrum that the material contains mainly Fe and trace of minor elements like Ca, K, Si and Mn.

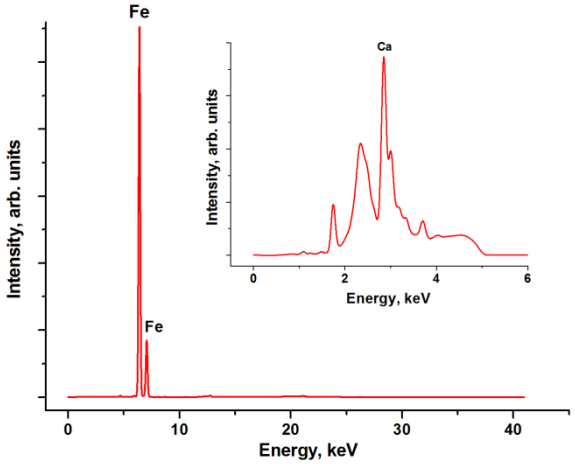

Fig.6. EDXRF of the obtained iron oxide material

The results can be described by the following model. Hexagonal closed-packed lattice of goethite with octahedrally coordinated iron ions and hydroxyl ions located between the oxygen planes during direct dehydratation transform to hematite. The formation of iron hydroxide according to the $Fe^{2+}/Fe^{3+}+OH^{-}\rightarrow Fe(OH)_2$ / $Fe(OH)_3$ equation is the first step of the material synthesis. At the next stage, the process strongly depends on the pH of the reaction medium and can be described as $Fe(OH)_2$ /$Fe(OH)_3$ $\rightarrow$ FeOOH at low pH and as $FeOOH + Fe^{2+} \rightarrow Fe_3O_4 + H^{+}$ at high pH [20]. In our case, for pH=5 –6 the process of magnetite formation is incomplete and the material consists of the particles where magnetite and goethite phases coexist. The spinel phase formation involves rearrangement of ions and protons transfer across the reaction interface. In partially transformed grain, magnetite nucleation involves Fe^{2+} so that the magnetite phase will grow from the surface part of particles to inner layers until magnetite core formation. In these conditions the resistivity of inter-grain boundaries partially formed by goethite is high. Coexistence of regions with low and high concentration of hydroxyl groups with acceptor and donor properties leads to the intensification of proton migration and enlarging both of particle's specific surface area and surface resistivity. According to low-temperature nitrogen absorption data the BET specific surface area of the investigated material is about 40 m^2/g. The disordering of Fe^{3+} and Fe^{2+} ions between oxygen layers was observed by Mossbauer spectroscopy and XRD.

The prepared material was primarily examined using optical microscopy. The sample was dispersed in ethanol using an ultrasonic bath for 15 min and then the suspension was spread on a glass surface. A microphotograph of the obtained powder on glass is presented in Fig. 7. It can be seen that the powder is characterized by a large number of particles with a diameter of less than 10 μm and irregular shape.

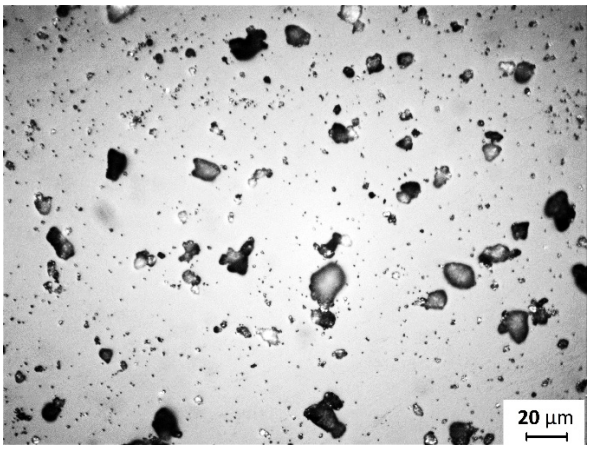

Fig.7 Microphotographs of magnetite powder particles

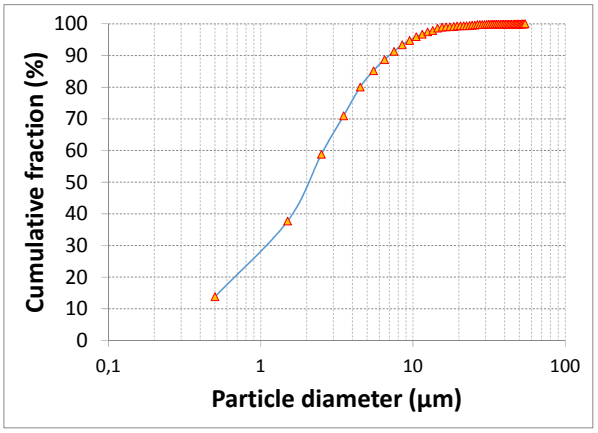

Fig. 8 Particle size distribution of magnetite

The determination of particle size and size distribution of our powders was based on the measurement of projected surface area of particles. One of the options the ImageJ program has is automatic determination of agglomerated particle size distributions using projected surface area. Equivalent spherical particle diameters can be calculated. The particle size distribution allows one to obtain the S-curve plot of cumulative number of agglomerates vs. their average diameters (Fig. 8). The average size of agglomerates varies from 0.5 to 50 μm when the sizes are mostly less than 7 μm. About 50% of the agglomerates particles have the particle size less than 2.2 μm.

Conclusions

An efficient and large-scale method for obtaining ultrafine magnetite using a green chemistry approach (a straightforward air-aqueous oxidation of St3 steel wastes) has been proposed. Reproducible scale-up of the material production up to 80 g per batch was successfully achieved. The synthesized iron oxides have BET specific surface area of about 40 m^2/g. The obtained material exhibits excellent magnetic properties and competitive conductivity values. Inexpensive magnetite powders with such degree of dispersion can be used in the production of alkaline Ni-Fe batteries, magnetic drives, ferrites, catalysts and materials for electromagnetic radiation protection [21].

References

[1] Z.Li, M. Kawashita, N.Araki, M. Mitsumori, M. Hiraoka, Journal of biomaterials applications 25(7) (2011) 643-661.
[2] Handbuch der Praparativen Anorgarlschen Chemie/ Ed. Georg Brauer, Verlag Stuttgart (1975)/ Translated and Published on Russian, Moscow, Myr, v. 5 (1885) 1751.
[3] http://metallicheckiy-portal.ru/marki_metallov/stk/St3spC.
[4] G. T. Brown, "X-ray diffraction procedures for clay mineral identification." Crystal structures of clay minerals and their X-ray identification (1980) 305-356.
[5] S. Kakuta, T. Numata, T. Okayama. Catalysis Science & Technology 4(1) (2014) 164-169.
[6] J. Rakovan, U. Becker, M.F. Hochella. American Mineralogist 84(5-6) (1999) 884-894.
[7] E.Wolska, U.Schwertmann, Zeitschrift für Kristallographie-Crystalline Materials 189(1-4) (1989) 223-238.
[8] V. Kotsyubynsky, V. Moklyak, A. Hrubiak, Materials Science-Poland 32.3 (2014) 481-486.
[9] G C. Aorski, M.M. Scherer, American Mineralogist 95(7) (2010) 1017-1026.
[10] G.M. da Costa, E. de Grave, R.E, Vandenberghe. Hyperfine Interactions 117 (1996) 207–243.
[11] R. E.Vandenberghe, C.A. Barrero, G.M. da Costa, E.Van San, E. de Grave, Hyperfine Interactions 126(1-4) (2000) 247-259.

[12] Murad Enver, American Mineralogist 67 (1982) 1007-1011.
[13] B. Lorenz, D. Ihle, Physica status solidi (b) 69(2) (1975) 451-457.
[14] N. Guskos, G.J. Papadopoulos, V. Likodimos, S. Patapis, Y. Darmis, A Przepiera, K. Aidinis, Materials Research Bulletin 37(6) (2002) 1051-1061.
[15] A. Radoń, D. Łukowiec, M. Kremzer, J. Mikuła, P. Włodarczyk, Materials (Basel, Switzerland) 11(5) (2018).
[16] J. R. Macdonald, Solid State Ionics 133(1-2) (2000) 79-97.
[17] Y. B.Taher, A. Oueslati, N.K. Maaloul, K. Khirouni, M. Gargouri, Applied Physics A 120(4) (2015) 1537-1543.
[18] R. M.Hill, L.A. Dissado, Journal of Physics C: Solid State Physics 18(19) (1985) 3829.
[19] S.R. Elliott, Advances in Physics 36(2) (1987) 135-217.
[20] Z.H. Zhou, J. Wang, X. Liu, H.S. Chan, Journal of Materials Chemistry 11(6) (2001) 1704-1709.
[21] Barsukov V, Senyk I, Kryukova O, Butenko O. Materials Today: Proceedings. Upcoming issue ICPAM-11 (2018) *(in print)*